Journal of Thermal Analysis and Calorimetry (2023) 148:12609–12627
https://doi.org/10.1007/s10973-023-12549-8

Numerical analysis of Marangoni convective flow of gyrotactic microorganisms in dusty Jeffrey hybrid nanofluid over a Riga plate with Soret and Dufour effects

Munawar Abbas[1] · Nargis Khan[1] · M. S. Hashmi[2] · Mustafa Inc[3,4,5]

Received: 23 May 2023 / Accepted: 31 August 2023 / Published online: 16 October 2023

Abstract

The proposed study explores the effects of thermo-solutal Marangoni convection on radiated Jeffrey fluid in the presence of gyrotactic microorganisms, nanoparticles and dust particles over a Riga plate. The Riga plate is composed of magnets and electrodes organized on a plate. The Lorentz force grows exponentially in the vertical direction because the fluid conducts electricity. The Dufour–Soret effects and activation energy are discussed in the present model. The molten crystal development, the expansion of vapor bubbles during nucleation, thin-film diffusion and semiconductor fabrication are few applications of Marangoni convection. We combined dust particles with microorganisms in present study to enhance the mass transport phenomena. The main objective of this study is to determine the thermal mobility of nanoparticles with $C_2H_6O_2$ ethylene glycol as base fluid. For the thermal analysis, Fe_3O_4 and Cu nanoparticles are more effective elements. With the use of new set of similarity variables, the governing PDEs are converted into ODEs, which are then numerically solved using the MATLAB (RKF-45th) technique. The results reveal that the velocity profiles rise for both the fluid and dust phases, while the thermal, microorganism and concentration profiles decline as the Marangoni convection parameter rises. By increasing the value of Marangoni convection parameter up to 10% the values of heat transfer and mass transfer enhance up to 9% and 7.15%, respectively.

Keywords Gyrotactic microorganisms · Jeffrey hybrid nanofluid · Activation energy · Soret and Dufour effects · Marangoni convection · Riga plate

List of symbols

C	Fluid phase concentration
N	Density of motile microorganism
k'	Chemical reaction co-efficient
L	Reference length
N_p	Density particle phase
m	Mass of dust particles
Ec	Eckert number
C_m	Specific heat of the dust particle
D_n	Diffusivity of microorganisms
q_r	Radiative heat flux
r_P	Radius of dust particles
D_m	Mass diffusivity coefficient/$\mathrm{m}^2\ \mathrm{s}^{-1}$
C_p	Specific heat of the fluid/$\mathrm{Jkg}^{-1}\mathrm{k}^{-1}$
C_p	Concentration of the particle phase
T_0	Constants
τ_m	Time required by the motile organisms
T_∞	Particle ambient temperature/k
Gr	Grashof number
T_P	Particle temperature
T_∞	Fluid ambient temperature
T	Fluid temperature/k
Le	Lewis number
k_f	Thermal conductivity of the fluid
B_0	Uniform magnetic field
Pe	Bioconvection Peclet number
Gn	Bioconvection mixed convection parameter

✉ Mustafa Inc
minc@firat.edu.tr

[1] Department of Mathematics, The Islamia University of Bahawalpur, Bahawalpur, Pakistan

[2] Department of Mathematics, The Government Sadiq College Women University, Bahawalpur, Pakistan

[3] Department of Computer Engineering, Biruni University, 34010 Istanbul, Turkey

[4] Department of Mathematics, Firat University, 23119 Elazig, Turkey

[5] Department of Medical Research, China Medical University, 40402 Taichung, Taiwan

Gc	Concentration mixed convection parameter
J_0	Extrinsic current density in the electrodes
Lb	Bio-convection Lewis number
p	Electrodes and magnets breadth
M_0	Permanent magnets magnetization
$\mathrm{Nn_x}$	Local density of motile microorganisms
N^*	Dust particle density
q_w	Heat flux $\mathrm{W\,m^{-2}}$
q_n	Motile microorganism's flux
Q	Hartman number
q_m	Mass flux $\mathrm{kg\,m^2s^{-1}}$
Rd	Thermal Radiation parameter
Ma	Marangoni convection parameter
Mn	Marangoni number
k^*	Mean absorption coefficient $\mathrm{cm^{-1}}$
σ_f	Electrical conductivity $\mathrm{sm^{-1}}$
A^*	Space-dependent heat source coefficient
B^*	Temperature-dependent heat source coefficient
(x, y)	Cartesian coordinates
(u, v)	Velocity fields of fluid $\mathrm{m\,s^{-1}}$
$\left(u_\mathrm{p}, v_\mathrm{p}\right)$	Velocity fields of particle phase $\mathrm{m.s^{-1}}$
$\mathrm{Nu_x}$	Nusselt number
$\mathrm{Sh_x}$	Sherwood number
C_fx	Skin friction
$K = 6\pi\mu r$	The coefficient of drag stokes
r	Radius of the dust particle
Pr	Prandtl number
M	Magnetic parameter
W_c	Maximum cell swimming speed
τ_T	Thermal relaxation time
$\psi(x, y)$	Streams functions of fluid phase
τ_C	Concentration relaxation time
ρ_f	Fluid density $\mathrm{kgm^{-3}}$
β_m	Fluid-particle interaction parameter for bio-convection
σ_1	Surface tension $\mathrm{Nm^{-1}}$
E_a	Activation energy coefficient $\mathrm{kgm^2s^{-2}}$
$\Psi(x, y)$	Streams functions of particle phase
τ_v	Momentum relaxation time
σ_0	Surface tension
ρ_P	Particle density
γ	Specific heat ratio
τ_w	Surface shear stress
β_T	Thermal dust parameter
v_f	Kinematic viscosity $\mathrm{m^2s^{-1}}$
β_v	Fluid-particle interaction parameter
β	Deborah number
β_1	Non-dimensionless constant
Rc	Chemical reaction parameter
ε_1	Variable thermal conductivity parameter
β_c	Parameter for fluid-particle interaction for concentration
λ_2	Ratio of the relaxation time to the retardation time
Ω	Microorganisms concentration difference parameter
k_f	Thermal conductivity of the fluid $\mathrm{Wm^{-1}k^{-1}}$
τ_v	Relaxation time of the dust particles
γ_T	Surface tension coefficients for temperature
B_0	Uniform magnetic field $\mathrm{kgs^{-2}A^{-1}}$
γ_C	Surface tension coefficients for concentration
σ^*	Stefan–Boltzmann constant $\mathrm{Wm^{-2}k^{-4}}$
λ_1	Retardation time
μ_f	Dynamic viscosity $\mathrm{kgm^{-1}s^{-1}}$

Superscript

$'$	Derivative with respect to ξ
f	Base fluid
hnf	Hybrid nanofluid
∞	Ambient
0	Surface

Introduction

The phenomenon that the liquid gravity predominated in natural convection and gradually dissipated in microgravity conditions was found by Marangoni in the middle of the 1860s. Surface tension has an important impact on the gradient of surface tension at the liquid interface. The study of mass and heat transfer in this marvel has garnered a lot of interest due to its numerous uses in the fields of nanotechnology, welding processes, silicon wafers, atomic reactors, thin film stretching, soap films, melting, semiconductor processing, crystal growth, and materials sciences. The solute Marangoni effect (EMS) and the thermal Marangoni effect (EMT) are the two classes into which the Marangoni effects are categorized. The thermal imbalance of the interfacial region, which is primarily based on the temperature gradient and heat source, is that leads to EMT. EMS is caused by the imbalance of the interfacial adsorption, which is due to chemical reactions and the concentration gradient. The modeling of the Marangoni effect was inspired by Pearson [1]. The deposition of thermophoretic particles in Carreau–Yasuda fluid across a chemically reactive Riga plate was studied by Abbas et al. [2]. The Marangoni convection boundary layer flow of a nanofluid is examined by Mat et al. [3]. The Marangoni convection flow and heat transmission properties of water-CNT nanofluid droplets were explored by Al-Sharafi et al. [4]. The pattern of generation of microorganism suspensions, such as bacteria and algae, can be interpreted as bioconvection. The occurrence of these self-moving, motile microbes raises the density of the primary fluid. There are wide range of uses of bioconvection, including organic applications and microsystems, the pharmaceutical industry, biopolymer manufacturing, economical energy sources, microbial progressed oil recovery, biotechnology and biosensor. Khan et al. [5] examined the numerical modeling and analysis of bioconvection on MHD flow due to an upper paraboloid surface of revolution. Chu et al. [6] investigated the study of nanofluid flow over a stretching disks in the presence of gyrotactic microorganisms. For further details, consider [7–10]. The concept "Arrhenius activation" was first used by Svante Arrhenius in 1889. When potential reactants are present in a chemical system, the least amount of energy is needed to initiate a reaction. The activation energy causes the atoms to move swiftly, which causes a reaction. The idea of activation energy is crucial in the field of chemistry. Many chemically reactive systems, including oil reservoirs and geothermal engineering, exhibit Arrhenius activation energy. A hybrid nanofluid MHD flow and heat transmission over a rotating disk were investigated by Reddy et al. [11] by taking Arrhenius energy into account. The effects of the binary chemical reaction and Arrhenius activation energy on the nanofluid flow were examined by Khan et al. [12].

Non-Newtonian fluids have an extensive range of industrial and technological uses, which causes an increase in researcher's interest. A number of models of non-Newtonian fluids have been put out in light of their deviations from Newtonian fluids. The most prevalent and fundamental model of non-Newtonian fluids is the Jeffrey fluid, which has a time derivative rather than a general derivative, and provides the best explanation of rheological viscoelastic fluids. Jeffrey fluid is more desirable in the polymer industry due to its linear viscoelastic behavior. Due to its viscoelastic properties, Jeffrey fluid is known to play a significant impact in blood flow and fluid mechanics. Being a considerable generalization of a Newtonian fluid, Jeffrey fluid can be obtained as a special case of Newtonian fluid. Hussain et al. [13] addressed the impacts of the thermal relaxation, double stratification and heat source on Jeffrey fluids flow. The heat transfer phenomena for the Jeffrey fluid flow along a stretched curved surface was solved by Ijaz Khan and Alzahrani [14] by using the shooting approach in the presence of activation energy and entropy minimization. Nanoparticles having sizes between 1 and 100 nm are suspended in a base fluid to develop nanofluids. Nanoparticles continue to have an impact in the varying physical properties of base liquids, such as thermal conductivity, density, electrical conductivity and viscosity. The impact of exponentially varying viscosity and permeability on the Blasius flow of Carreau nanofluid over an electromagnetic plate via a porous media was examined by Hakeem et al. [15]. The effects of nonlinear radiation on magnetic and non-magnetic nanoparticles with various base fluids were studied by Saranya et al. [16] over a flat plate. The flow of nanofluids and its industrial and nuclear applications have attracted the attention of many researchers [17–23]. In comparison with base liquids and other nanofluids, hybrid nanofluids have a higher thermal conductivity. Hybrid nanofluids have dissimilar applications when compared to nanofluids. By combining two different kinds of nanoparticles with the base liquid, hybrid nanofluids are produced. The numerical simulation of surface tension flow of hybrid nanofluid over an infinite disk with thermophoresis particle deposition was investigated by Abbas et al. [24]. Acharya [25] investigated the magnetized hybrid nanofluid flow and associated thermal boundary conditions within a cube equipped with a circular cylinder. The flow of hybrid nanofluids and its applications have attracted the attention of numerous researchers [26–29]. Figures 1 and 2 show the applications of nanofluids and hybrid nanofluid respectively. Figure 3 displays the manufacturing process for nanofluids and hybrid nanofluids.

The Dufour effect is the term given to the heat transfer induced by a concentration gradient as compared to the Soret effect, which is the term given to the mass transfer caused by temperature gradient. For isotope separation and in a combination of gases with light and medium molecular mass, the Soret effect is used. The impact of Dufour and Soret on mass and heat transmission was examined by Postelnicu [30]. The effects of Dufour and Soret on mixed convection in a non-Darcy porous media saturated with micro-polar fluid were studied by Srinivasacharya and Reddy [31]. As a result, [32–35] show an exploration of this topic from several physical aspects. The Riga plate is a collection of alternating electrodes as well as permanent magnets that are mounted on a flat surface to guarantee efficient flow within the electromagnetic motor. Riga is a spanwise-replaced permanent magnetization device that is operated by electromagnetics. The Riga plate design generates a Lorentz force that reduces exponentially, which causes the flow to go through the plate. It is the Riga plate that is a great device to stop the separation of the boundary layer and reduce the amount of turbulence. It creates the crossing of electric and magnetic fields which are fixed to an even surface. The non-uniform heat source effects on the 3-D flow of nanoparticles with various base fluids past a Riga plate are examined by Ragupathi et al. [36]. For further details, consider [37–42].

The analysis of above literature reveals that none of the studies has been conducted yet to explore the effect of thermo-solutal Marangoni convection on dusty Jeffrey hybrid nanofluid flow across a Riga plate with gyrotactic microorganisms. The present investigation is an extension of Mamatha et al. [43] and fills this gap. The effects of a magnetic field, viscous dissipation, a non-uniform heat source and activation energy are also investigated. Combining Fe_3O_4 and Cu particles with an ethylene glycol ($C_2H_6O_2$) base fluid is claimed to develop the characteristics of the hybrid nanofluid. Using RKF-45th method, numerical

Fig. 1 Applications of nanofluids

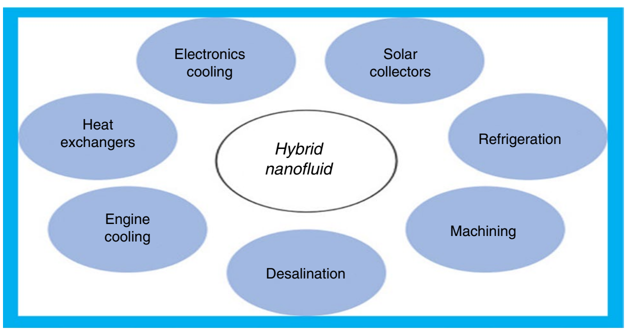

Fig. 2 Applications of hybrid nanofluids

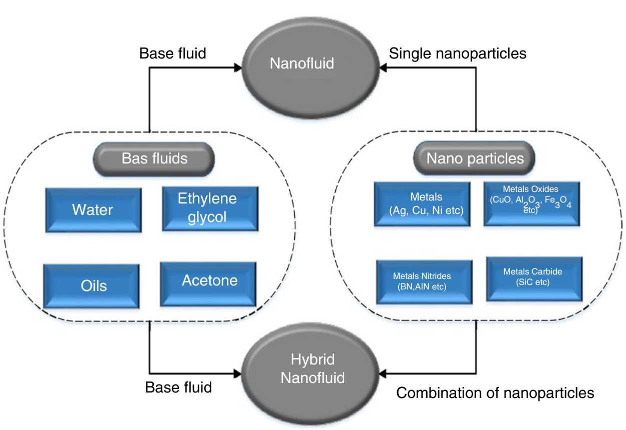

Fig. 3 Manufacturing procedure for nanofluids and hybrid nanofluids

solution is assembled. The purposes of the analysis are as follows:

- The goal of this research is to ascertain how thermo-solutal Marangoni convection affects the temperature, microbe, flow, and concentration profiles of the dusty Jeffrey hybrid nanofluid.
- To determine how the thermal boundary layer of Jeffrey hybrid nanofluid and dust particles is impacted by the heat generation/absorption.
- Examine the impact of the activation energy parameter on the dust and fluid phase concentration profiles.
- The purpose of this examination is to explore the impacts of Dufour and Soret on the thermal and concentration boundary layer flow of dusty hybrid nanofluid.

Mathematical formulation

The thermo-solutal Marangoni convective flow of a dusty Jeffrey hybrid nanofluid including microorganisms across a Riga plate has been taken into consideration. The geometric profile of the current model is shown in Fig. 4. The effects of Soret and Dufour have been observed extensively. The present model is described as: (i) Variable thermal conductivity is assumed. (ii) The study is conducted with mixed convection and activation energy. (iii) B_0 is a constant magnetic field that is applied along the $y-$ axis. (iv) We assume non-uniform heat generation/absorption and viscous dissipation. (v) Dust and nanoparticles, which are spherical in shape, are deliberated to be evenly distributed throughout the fluid. (vi) Thermal properties and correlations of Fe_3O_4

Fig. 4 Flow description

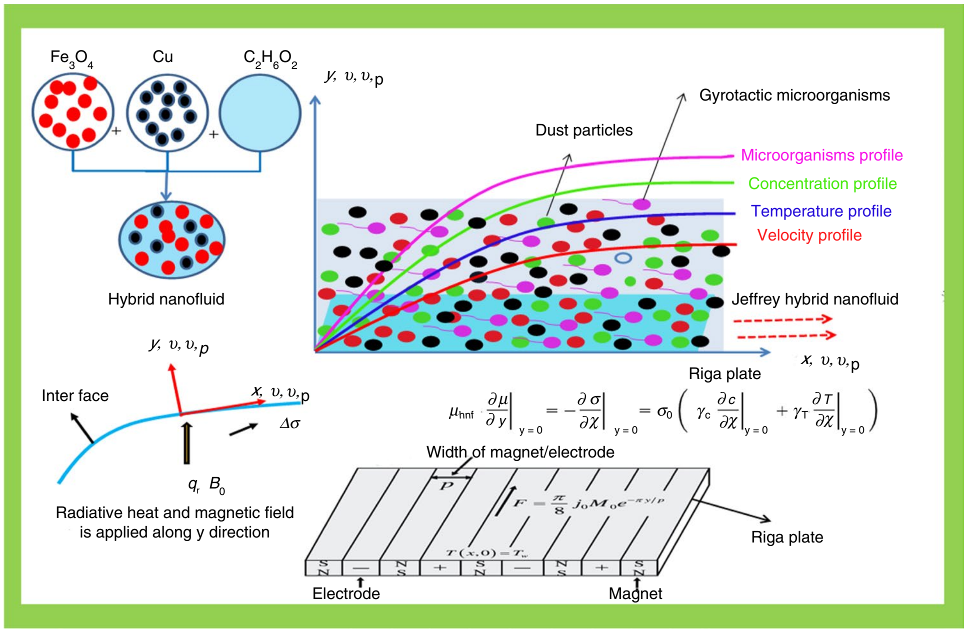

Fig. 5 Applications of Cu nanoparticles

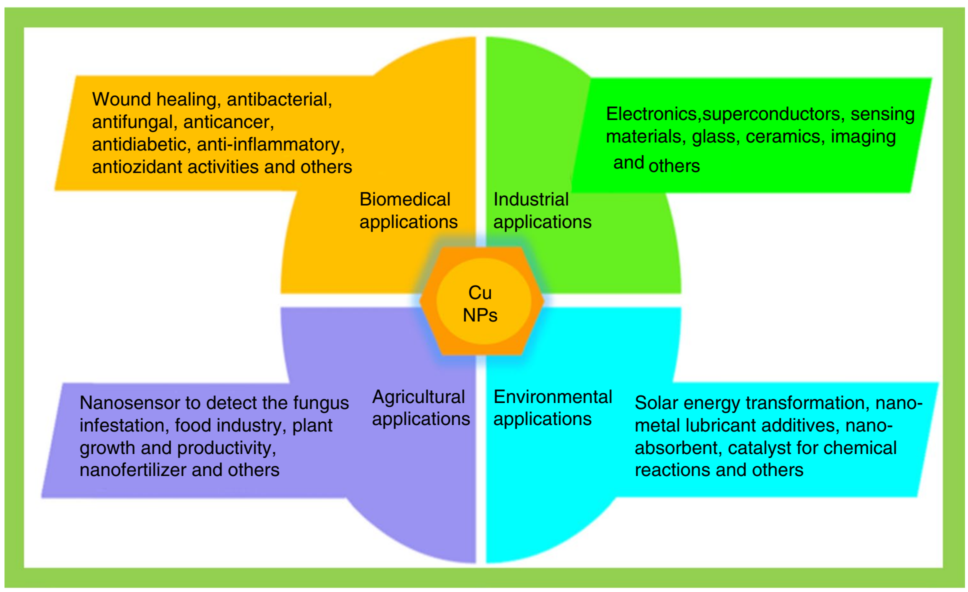

and $Fe_3O_4 + Cu$ in $C_2H_6O_2$. (vii) The dusty fluid moves at a similar velocity as the movable microorganisms. Figures 5 and 6 express the applications chart of Cu and Fe_3O_4 nanoparticles, respectively.

Riga plate

According to Abbas et al. [2], the Lorentz force F of the Riga plate is as follows:

$$F = \frac{M_0 J_0 \pi}{8} \exp\left[-y\frac{\pi}{p}\right]. \tag{1}$$

Heat source

In the current model, the term q''' is described as a heat source/sink (Obalalu et al. [44]):

$$q''' = \frac{K_{\mathrm{hnf}}(T)\rho_{\mathrm{hnf}}U_0}{2\mu_{\mathrm{hnf}}X}\left[A^* T_0 X^2 f' + B^*\left(T - T_\infty\right)\right]. \tag{2}$$

Thermal conductivity

The following concept applies to the thermal conductivity (Obalalu et al. [44]):

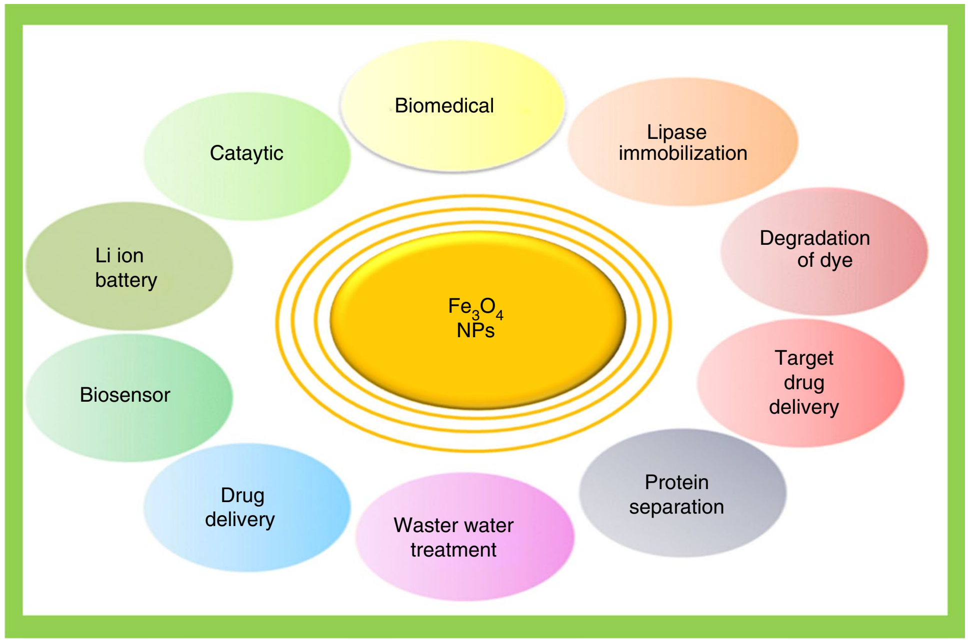

Fig. 6 Applications of Fe_3O_4 nanoparticles

$$K^*(T) = k_{\mathrm{hnf}}\left[1 + \varepsilon\left(\frac{T - T_\infty}{T_0 X^2}\right)\right] \tag{3}$$

Marangoni convection

The surface tension $\sigma_1 = \sigma_0\left[1 - \gamma_{\mathrm{T}}(T - T_\infty) - \gamma_{\mathrm{C}}(C - C_\infty)\right]$ is supposed to be dependent on linear alternation with solutal and thermal boundaries (see Abbas et al. [2]). Where the surface tension coefficients for concentration $\gamma_{\mathrm{C}} = -\frac{\partial\sigma_1}{\partial C}\Big|_{\mathrm{T}}$ and temperature is $\gamma_{\mathrm{T}} = -\frac{\partial\sigma_1}{\partial T}\Big|_{\mathrm{C}}$.

Model equations

The constitutive equations of microorganisms, momentum, continuity, concentration and energy for the analysis of the current flow in the fluid phase (Phase-I) and dust phase (Phase-II) are as follows (see Mamatha et al. [43], Gorla [44]):

Fluid phase

$$\frac{\partial u}{\partial x} + \frac{\partial v}{\partial y} = 0, \tag{4}$$

$$\begin{aligned}
&\rho_{\mathrm{hnf}}\left(u\frac{\partial u}{\partial x} + v\frac{\partial u}{\partial y}\right) \\
&= \frac{\mu_{\mathrm{hnf}}}{1+\lambda_2}\left\{\frac{\partial^2 u}{\partial y^2} + \lambda_1\left(u\frac{\partial^2 u}{\partial x\partial y} - \frac{\partial u}{\partial x}\frac{\partial^2 u}{\partial y^2} + \frac{\partial u}{\partial y}\frac{\partial^2 u}{\partial x\partial y} + v\frac{\partial^2 u}{\partial y^2}\right)\right\} \\
&\quad + KN(u_{\mathrm{p}} - u) - \sigma_{\mathrm{hnf}}B_0^2 u + \frac{\pi j_0 M_0 \exp\left(-\frac{\pi}{p}y\right)}{8} \\
&\quad + g(\rho\beta^*)_{\mathrm{hnf}}\left((1 - C_\infty)(T - T_\infty) - (\rho_{\mathrm{p}} - \rho_{\mathrm{f}})(C - C_\infty) - (\rho_{\mathrm{p}} - \rho_{\mathrm{f}})(N - N_\infty)\right),
\end{aligned} \tag{5}$$

$$\begin{aligned}
&(\rho c_{\mathrm{p}})_{\mathrm{hnf}}\left(u\frac{\partial T}{\partial x} + v\frac{\partial T}{\partial y}\right) \\
&= \frac{\partial}{\partial y}\left(K^*(T)\frac{\partial T}{\partial y}\right) + \frac{16\sigma^* T_\infty^3}{3k^*}\frac{\partial^2 T}{\partial y^2} \\
&\quad + \frac{\rho_{\mathrm{p}C_{\mathrm{m}}}}{\tau_{\mathrm{t}}}(T_{\mathrm{P}} - T) \\
&\quad + \frac{\rho_{\mathrm{p}}}{\tau_{\mathrm{v}}}(u_{\mathrm{p}} - u)^2 + \left(\frac{\rho D_{\mathrm{m}} k_{\mathrm{T}}}{C_{\mathrm{s}}}\right)\frac{\partial^2 C}{\partial y^2} + q''' \\
&\quad + \frac{\mu_{\mathrm{hnf}}}{(1+\lambda_2)}\left\{\left(\frac{\partial u}{\partial y}\right)^2 + \lambda_1\left(u\frac{\partial u}{\partial y}\frac{\partial^2 u}{\partial y\partial x} + v\frac{\partial u}{\partial y}\frac{\partial^2 u}{\partial y^2}\right)\right\},
\end{aligned} \tag{6}$$

$$\begin{aligned}
u\frac{\partial C}{\partial x} + v\frac{\partial C}{\partial y} &= D_{\mathrm{m}}\frac{\partial^2 C}{\partial y^2} + \frac{\rho_{\mathrm{p}}}{\rho\tau_{\mathrm{C}}}(C_{\mathrm{p}} - C) \\
&\quad + \frac{D_{\mathrm{m}}k_{\mathrm{T}}}{T_{\mathrm{m}}}\frac{\partial^2 T}{\partial y^2} - k_{\mathrm{r}}^2(C - C_\infty)\left(\frac{T}{T_\infty}\right)^{\mathrm{m}}\exp\left(\frac{-E_{\mathrm{a}}}{k'T}\right),
\end{aligned} \tag{7}$$

$$\begin{aligned}
u\frac{\partial N}{\partial x} + v\frac{\partial N}{\partial y} &= D_{\mathrm{n}}\frac{\partial^2 N}{\partial y^2} - \frac{bW_{\mathrm{c}}}{(C_{\mathrm{w}} - C_\infty)}\left[\frac{\partial N}{\partial y}\frac{\partial C}{\partial y} + N\frac{\partial^2 C}{\partial y^2}\right] \\
&\quad + \frac{\rho_{\mathrm{p}}}{\rho\tau_{\mathrm{m}}}(N_{\mathrm{p}} - N),
\end{aligned} \tag{8}$$

Dust phase

$$\frac{\partial u_{\mathrm{p}}}{\partial x} + \frac{\partial v_{\mathrm{p}}}{\partial y} = 0, \tag{9}$$

$$u_{\mathrm{p}}\frac{\partial u_{\mathrm{p}}}{\partial x} + v_{\mathrm{p}}\frac{\partial u_{\mathrm{p}}}{\partial y} = \frac{K}{m}(u - u_{\mathrm{p}}), \tag{10}$$

$$\rho_p C_m\left(u_p\frac{\partial T}{\partial x}+v_p\frac{\partial T}{\partial y}\right)=\frac{\rho_p C_m}{\tau_T}(T-T_P), \tag{11}$$

$$u_p\frac{\partial C_p}{\partial x}+v_p\frac{\partial C_p}{\partial y}=\frac{1}{\tau_c}(C-C_p), \tag{12}$$

$$u_p\frac{\partial N_p}{\partial x}+v_p\frac{\partial N_p}{\partial y}=\frac{1}{\tau_m}(N-N_p), \tag{13}$$

The following are the possible boundary conditions for this problem (see Abbas et al. [24], Mamatha et al. [43], Gorla [45]):

$$\mu_{hnf}\frac{\partial u}{\partial y}=\frac{\partial \sigma_1}{\partial x}=-\sigma_0\left(\gamma_T\frac{\partial T}{\partial x}+\gamma_C\frac{\partial C}{\partial x}\right),\quad v=0,\quad \text{at}\quad y=0, \tag{14}$$

$$u\to 0,\quad u_p\to 0,\quad v_p\to v,\quad \text{at}\quad y\to\infty, \tag{15}$$

$$T=T_\infty+T_0X^2,\ \text{at}\quad y=0, T\to T_\infty,\quad T_p\to T_\infty\ \text{at}\quad y\to\infty, \tag{16}$$

$$C=C_\infty+C_0X^2,\ \text{at}\quad y=0,\quad C\to C_\infty,\quad C_p\to C_\infty,\ \text{at}\quad y\to\infty, \tag{17}$$

$$N=N_\infty+N_0X^2,\ \text{at}\quad y=0,\quad N\to N_\infty,\quad N_p\to N_\infty,\ \text{at}\quad y\to\infty. \tag{18}$$

where this term $\frac{16\sigma^* T_\infty^3}{3k^*}\frac{\partial^2 T}{\partial y^2}$ in Eq. (6) represents thermal radiation, the term $\frac{\rho_p c_m}{\tau_t}(T_P-T)$ in Eq. (6) represents two phase flow temperature difference, the term $\left(\frac{\rho D_m k_T}{C_s}\right)\frac{\partial^2 C}{\partial y^2}$ Eq. (6) represents Dufour effect, term q''' in Eq. (6) represents non-uniform heat source, the term $\frac{\mu_{hnf}}{(1+\lambda_2)}\left\{\left(\frac{\partial u}{\partial y}\right)^2+\lambda_1\left(u\frac{\partial u}{\partial y}\frac{\partial^2 u}{\partial y\partial x}+v\frac{\partial u}{\partial y}\frac{\partial^2 u}{\partial y^2}\right)\right\}$ in Eq. (6) represents viscous dissipation, the term $\frac{D_m k_T}{T_m}\frac{\partial^2 T}{\partial y^2}$ in Eq. (7) represents Soret effect, the term $k_r^2(C-C_\infty)\left(\frac{T}{T_\infty}\right)^m\exp\left(\frac{-E_a}{k'T}\right)$ in Eq. (7) represents activation energy term, and the term $\frac{\rho_p}{\rho\tau_C}(C_p-C)$ in Eq. (7) represents concentration difference of two phase flow.

Similarity transformations

Introduce the following transformations (see Mamatha et al. [43], Gorla [45]):

$$\psi(x,y)=v_f X f(\xi),\quad \Psi(x,y)=v_f X g(\xi), \tag{19}$$

$$u=\frac{\partial\psi}{\partial y},\quad u_p=\frac{\partial\Psi}{\partial y},\quad v=-\frac{\partial\psi}{\partial x}\ \text{and}\ v_p=-\frac{\partial\Psi}{\partial x}, \tag{20}$$

$$X=\frac{x}{L},\xi=\frac{y}{L},\quad T(x,y)=T_\infty+T_0X^2\theta(\xi),\quad T_P(x,y)=T_\infty+T_0X^2\theta_P(\xi), \tag{21}$$

$$C(x,y)=C_\infty+C_0X^2\phi(\xi),\quad C_P(x,y)=C_\infty+C_0X^2\phi_P(\xi), \tag{22}$$

$$N(x,y)=N_\infty+N_0X^2\Theta(\xi),\quad N_P(x,y)=N_\infty+N_0X^2\Theta_P(\xi),\ \rho_p=mN \tag{23}$$

The following fluid and particle phase Eqs. (19–23) can be put into Eqs. (7–21) to obtain the system of ODEs.

Phase-I

$$A_1\left(f'''+\beta\left((f'')^2-ff''''\right)\right)+A_2\left(f''f-(f')^2\right)+\beta_v l(g'-f')-A_3Mf'-+A_4\mathrm{Gr}(\theta+\mathrm{Gc}\phi+\mathrm{Gn}\Theta)+\mathrm{Q}e^{-\beta\eta}=0, \tag{24}$$

$$A_5\left(\theta''(1+\varepsilon\theta)+\varepsilon(\theta')^2\right)+\mathrm{Rd}\theta''+A_6\mathrm{Pr}\left(f\theta'-2f'\theta\right)+\mathrm{Pr}\gamma l\beta_t\left[\theta_p-\theta\right]+\mathrm{PrEc}\beta_v l(g'-f')^2+\mathrm{PrEc}A_1\left((f'')^2+\beta\left((f'')^2f'-ff''f'''\right)\right)+\mathrm{DuPr}\phi''+\frac{A_2A_5(1+\varepsilon\theta)}{A_1}\left(A^*f'+B^*\theta\right)=0, \tag{25}$$

$$\phi''+\mathrm{Le}\left(f\phi'-2f'\phi\right)+\mathrm{Le}l\beta_c\left[\phi_p-\phi\right]-\mathrm{LeRc}(1+\delta\theta)e^{\frac{-\mathrm{E}}{(1+\delta\theta)}}\phi+\mathrm{LeSr}\theta''=0, \tag{26}$$

$$\Theta''+\mathrm{Pe}\left[\Theta'\phi'+(\Omega+\Theta)\phi''\right]+Lbf\Theta'+l\beta_m Lb\left[\Theta_p-\Theta\right]=0, \tag{27}$$

Phase-II

$$gg''-g'^2+\beta_v\left[f'-g'\right]=0, \tag{28}$$

$$g\theta_p'-2g'\theta_p+\beta_t\left[\theta-\theta_p\right]=0, \tag{29}$$

$$g\phi_p'-2g'\phi_p+\beta_c\left[\phi-\phi_p\right]=0, \tag{30}$$

$$g\Theta_p'-2g'\Theta_p+\beta_m\left[\Theta-\Theta_p\right]=0. \tag{31}$$

Boundary conditions

$$f''(0) = -\frac{2\mathrm{Mn}(1 + \mathrm{Ma})}{A_1}, \quad f(0) = 0, \tag{32}$$

$$f'(\infty) = 0, \quad f''(\infty) = 0, \quad g'(\infty) = 0, \quad g(\infty) = f(\infty), \tag{33}$$

$$\theta(0) = 1, \quad \theta(\infty) = 0, \quad \theta_{\mathrm{p}}(\infty) = 0, \tag{34}$$

$$\phi(0) = 1, \quad \phi(\infty) = 0, \quad \phi_{\mathrm{p}}(\infty) = 0, \tag{35}$$

$$\Theta(0) = 1, \quad \Theta(\infty) = 0, \quad \Theta_{\mathrm{p}}(\infty) = 0. \tag{36}$$

where magnetic parameter, microorganism mixed convection parameter, fluid-particle interaction parameter, Dufour number, dust particles mass concentration parameter, relaxation time of the dust particles, solutal mixed convection parameter, Marangoni ratio parameter, Marangoni number, Prandtl number, fluid-particle interaction parameter for temperature, Lewis number, fluid interaction parameter for concentration, thermal mixed convection parameter, Peclet number, thermal radiation parameter, fluid interaction parameter for bio-convection, Soret number, microorganisms concentration difference parameter, chemical reaction parameter, specific heat ratio, activation energy parameter, Deborah number, bio-convection Lewis number, Hartman number are given below.

$$M = \frac{\sigma_{\mathrm{f}} B_0^2 L^2}{\nu_{\mathrm{f}}}, \ \mathrm{Gn} = \frac{\beta_{\mathrm{n}}^* N_0}{\beta T_0}, \ \beta_{\mathrm{v}} = \frac{L}{\tau_{\mathrm{v}}},$$
$$l = \frac{Nm}{\rho_{\mathrm{f}}}, \ \mathrm{Du} = \frac{\rho k_{\mathrm{t}} D_{\mathrm{m}} C_0}{C_{\mathrm{S}} C_{\mathrm{p}} T_{\mathrm{o}}}, \ \tau_{\mathrm{v}} = \frac{m}{K},$$
$$\mathrm{Gc} = \frac{\beta_{\mathrm{c}}^* C_0}{\beta T_0}, \ \mathrm{Ma} = \frac{C_0 \gamma_{\mathrm{c}}}{T_0 \gamma_{\mathrm{T}}}, \ \mathrm{Mn} = \frac{\sigma_0 T_0 \gamma_{\mathrm{T}} L}{\mu_{\mathrm{f}} \nu_{\mathrm{f}}}$$
$$\mathrm{Pr} = \frac{\mu_{\mathrm{f}} C_{\mathrm{p}}}{K_{\mathrm{f}}}, \ \mathrm{Le} = \frac{\alpha_{\mathrm{f}}}{D_{\mathrm{m}}}, \ \beta_{\mathrm{c}} = \frac{L^2}{\nu_{\mathrm{f}} \tau_{\mathrm{c}}}$$
$$\mathrm{Gr} = \frac{g T_0 L^2 (\rho\beta)_{\mathrm{f}}}{\rho_{\mathrm{f}} \nu_{\mathrm{f}}}, \ \beta_{\mathrm{t}} = \frac{L^2}{\nu_{\mathrm{f}} \tau_{\mathrm{t}}}, \ \mathrm{Pe} = \frac{bWc}{D_{\mathrm{n}}},$$
$$\mathrm{Rd} = \frac{4\sigma^* T_\infty^3}{k^* k}, \ \beta_{\mathrm{m}} = \frac{L^2}{\nu_{\mathrm{f}} \tau_{\mathrm{m}}}, \ \mathrm{Sr} = \frac{k_{\mathrm{t}} D_m T_0}{T_{\mathrm{m}} C_0},$$
$$\Omega = \frac{N_\infty}{\left(N_{\mathrm{w}} - N_\infty\right)}, \ \mathrm{Rc} = \frac{L^2 K_{\mathrm{r}}^2}{\nu_{\mathrm{f}}}, \ \gamma = \frac{C_{\mathrm{m}}}{C_{\mathrm{p}}}, \ E = \frac{\mathrm{Ea}}{k^* T_\infty},$$
$$\beta = \frac{\lambda_1 \nu_{\mathrm{f}}}{L^2}, \mathrm{Lb} = \frac{\alpha_{\mathrm{f}}}{D_{\mathrm{n}}} \text{and } Q = \frac{M_0 L^3 \pi J_0}{8\nu^2}.$$

Physical curiosity

For non-Newtonian fluid (Jeffrey hybrid nanofluid), the $\mathrm{Nu_x}$ local rate of heat transfer, $\mathrm{Nn_x}$ density of motile microorganisms, $\mathrm{Sh_x}$ local rate of mass transfer and C_{fx} local skin friction are addressed.

$$C_{\mathrm{fx}} = \frac{\tau_{\mathrm{w}}}{\rho}, \ \mathrm{Nu_x} = \frac{x q_{\mathrm{w}}}{k_{\mathrm{f}}\left(T_{\mathrm{w}} - T_\infty\right)},$$
$$\mathrm{Sh_x} = \frac{x q_{\mathrm{m}}}{D_{\mathrm{m}}\left(C_{\mathrm{w}} - C_\infty\right)}, \tag{37}$$
$$\mathrm{Nn_x} = \frac{x q_{\mathrm{n}}}{D_{\mathrm{n}}\left(N_{\mathrm{w}} - N_\infty\right)},$$

$$\tau_{\mathrm{w}} = \frac{\mu_{\mathrm{hnf}}}{1 + \lambda_2}\left[\frac{\partial u}{\partial y} + \lambda_1\left\{u\frac{\partial^2 u}{\partial y \partial x} + v\frac{\partial^2 u}{\partial y^2}\right\}\right]_{y=0}, \tag{38}$$

$$q_{\mathrm{w}} = -\left[k_{\mathrm{hnf}}\left(1 + \varepsilon\left(\frac{T - T_\infty}{T_0 X^2}\right)\right) + \frac{16 T_\infty^3 \sigma^*}{3k^*}\right]\frac{\partial T}{\partial y}\bigg|_{y=0}, \tag{39}$$

$$q_{\mathrm{m}} = -D_{\mathrm{m}}\frac{\partial C}{\partial y}\bigg|_{y=0}, \quad q_{\mathrm{n}} = -D_{\mathrm{n}}\frac{\partial N}{\partial y}\bigg|_{y=0}, \tag{40}$$

$$\mathrm{C_{fx}}\left(\mathrm{Re_x}\right)^{-0.5} = \frac{A_1}{1 + \lambda_2}\left(f'' + \beta\left(f'(0)f''(0) - f(0)f'''(0)\right)\right), \tag{41}$$

$$\mathrm{Nu_x}\left(\mathrm{Re_x}\right)^{-0.5} = -\left(A_5(1 + \in \theta) + \mathrm{Rd}\right)\theta'(0), \tag{42}$$

$$\mathrm{Sh_x}\left(\mathrm{Re_x}\right)^{-0.5} = -\phi'(0), \quad \mathrm{Nn_x}\left(\mathrm{Re_x}\right)^{-0.5} = -\Theta'(0). \tag{43}$$

The thermo-physical features of hybrid nanofluid are shown in Table 1. The thermo-physical characteristics of base fluid and nanoparticles are displayed in Table 2.

Numerical method

The nonlinear BVP is reduced into a sequence of single-order IVP, and the RKF-45th approach is used to solve the problem. Add the following variables to the equations now:

$$u_1 = f, \quad u_2 = f', \quad u_3 = f'', \quad u_4 = f''', \quad u_4' = f'''', \tag{44}$$

$$u_5 = g, \quad u_6 = g', \quad u_6' = g'', \tag{45}$$

$$u_7 = \theta, \quad u_8 = \theta', \quad u_8' = \theta'' \tag{46}$$

$$u_9 = \theta_{\mathrm{p}}, \quad u_9' = \theta_{\mathrm{p}}'. \tag{47}$$

$$u_{10} = \phi, \quad u_{11} = \phi', \quad u_{11}' = \phi'', \tag{48}$$

Table 1 Base fluid and nanoparticle thermo-physical characteristics (Unyong et al. [46])

Properties constituents	c_p/J kg-1 K^{-1}	k/W $m^{-1}K^{-1}$	$\sigma/\Omega m^{-1}$	β/1 K^{-1}	ρ/kg m^{-3}
Fe_2O_4	670	6	25000	1.3	5200
Cu	385	401	5.96×10^7	1.67	8933
$C_2H_6O_2$	2415	0.252	5.5×10^{-6}	5.7	1114

$$u_{12} = \phi_p, \quad u'_{12} = \phi'_p. \tag{49}$$

$$u_{13} = \Theta, \quad u_{14} = \Theta', \quad u'_{14} = \Theta'', \tag{50}$$

$$u_{15} = \Theta_p, \quad u'_{15} = \Theta'_p. \tag{51}$$

$$u'_1 = u_2, \quad u'_2 = u_3 \quad u'_3 = u_4 \tag{52}$$

$$\begin{aligned} u'_4 =& \frac{1}{u_1 \beta A_1} \\ &\left(A_2\left(u_2^2 - u_1 u_3\right) + u_3 u_7 \varepsilon_1 e^{-u_6 \varepsilon_1} + L\beta_v\left(u_5 - u_2\right) + A_3 M u_2\right. \\ &\left. + - A_4 \mathrm{Gr}\left(u_7 + \mathrm{Gc}\, u_{10} + \mathrm{Gn} u_{13}\right) + u_4 A_1 + \beta A_1 (u_3)^3 - Qe^{-\beta\eta}\right) \end{aligned} \tag{53}$$

$$u'_5 = u_6, \quad u'_6 = u_5^{-1}\left(u_6^2 + \beta_v\left(u_6 - u_2\right)\right), \tag{54}$$

$$u'_7 = u_8, \tag{55}$$

$$\begin{aligned} u'_8 =& (A_5\left(1 + \varepsilon u_7\right) + \mathrm{Rd})^{-1}(-\varepsilon A_5 u_8^2 + A_6\left(\Pr(2\, u_2 u_7 - u_1 u_8\right) + \Pr L\gamma \beta_T\left(u_7 - u_9\right) \\ &- \Pr L E c \beta_v (u_6 - u_2)^2 - \frac{A_5 A_2 (1 + \varepsilon u_7)}{A_1}\left(A^* u_2 + B^* u_7\right) \\ &- \mathrm{Du} \Pr u'_{11} - \Pr \mathrm{Ec} A_1 ((u_3)^2 + \beta\left(u_2\left(u_3\right)^2 - u_1 u_3 u_4\right)) \end{aligned} \tag{56}$$

$$u'_9 = u_5^{-1}\left(2u_6 u_9 + \beta_T\left(u_9 - u_7\right)\right), \tag{57}$$

$$\begin{aligned} u'_{10} =& u_{11,} \\ u'_{11} =& \left(\left(\mathrm{Le}(2\, u_2 u_{10} - u_1 u_{11}\right) + \mathrm{Le}\beta_C L\left(z_{10} - z_{12}\right)\right. \\ &- \mathrm{LeSr} u'_7 + \mathrm{LeRc}\left(1 + \delta u_7\right) e^{\frac{-E}{(1+\delta\, u_7)}} \end{aligned} \tag{58}$$

$$u'_{12} = u_5^{-1}\left(2u_5 u_{12} + \beta_T\left(u_{12} - u_{10}\right)\right). \tag{59}$$

$$\begin{aligned} u'_{13} =& u_{14,} \\ u'_{14} =& \left(\left(\mathrm{Lb}(2u_2 u_{13} - u_1 u_{14}\right) + \mathrm{Lb}\beta_m L\left(u_{13} - u_{15}\right)\right. \\ &+ \mathrm{Pe}\left(u_{14} u_{11} + \left(\Omega + u_{13}\right) u'_{11}\right), \end{aligned} \tag{60}$$

$$u'_{15} = u_5^{-1}\left(2u_6 u_{15} + \beta_m\left(u_{15} - u_{13}\right)\right). \tag{61}$$

Boundary conditions

$$\begin{aligned} &u_1(0) = 0, \quad u_2(0) = n_1, \quad u_3(0) = -2\frac{\mathrm{Mn}(1 + \mathrm{Ma})}{e^{-u_6 \varepsilon_1} A_1}, \\ &u_3(0) = n_2, \quad u_5(0) = n_3, \end{aligned} \tag{62}$$

$$z_6(0) = n_4, \quad u_7(0) = 1, \quad u_7(0) = n_5, \quad u_9(0) = n_6, \tag{63}$$

Table 2 Represents the thermo-physical aspects of hybrid nanofluid (see Abbas et al. [24])

Properties	Hybrid nanofluid
Dynamic viscosity μ_{hnf}	$A_1 = \frac{\mu_{hnf}}{\mu_f} = \frac{1}{(1-\Phi_1)^{2.5}(1-\Phi_2)^{2.5}}$
Density ρ_{hnf}	$A_2 = \frac{\rho_{hnf}}{\rho_f} = \left[\Phi_2 \frac{\rho_{s_2}}{\rho_f} + \left(1 - \Phi_2\right)\left\{\Phi_1 \frac{\rho_{s_1}}{\rho_f} + \left(1 - \Phi_1\right)\right\}\right]$
Electrical conductivity σ_{hnf}	$A_3 = \frac{\sigma_{hnf}}{\sigma_{nf}} \times \frac{\sigma_{nf}}{\sigma_f} = \frac{\sigma_{lnf}}{\sigma_{bf}} = \left[\frac{\sigma_{s2}+(S-1)\sigma_{nf}-(S-1)\Phi_2\left(\sigma_{nf}-\sigma_{s2}\right)}{\left(\sigma_{nf}-\sigma_{s2}\right)\Phi_2+\sigma_{nf}+\sigma_{s2}}\right] \times \left[\frac{\sigma_{s1}+\sigma_f-\Phi_1\left(\sigma_f-\sigma_{s1}\right)}{\sigma_f+\Phi_1\left(\sigma_f-\sigma_{s1}\right)+\sigma_{s1}}\right]$
Thermal expansion coefficient $(\rho\beta)_{hnf}$	$A_4 = \frac{(\rho\beta)_{hnf}}{(\rho\beta)_f} = \left[\Phi_2 \frac{(\rho\beta)_{s_2}}{(\rho\beta)_f} + \left(1 - \Phi_2\right)\left\{\Phi_1 \frac{(\rho\beta)_{s_1}}{(\rho\beta)_f} + \left(1 - \Phi_1\right)\right\}\right]$
Thermal conductivity k_{hnf}	$A_5 = \frac{k_{hnf}}{k_{nf}} \times \frac{k_{nf}}{k_f} = \frac{\left(k_{s_2} + (S-1)k_{nf}\right) - (S-1)\Phi_2\left(k_{nf} - k_{s_2}\right)}{\left(k_{s_2} + (S-1)k_f\right) + \Phi_2\left(k_{nf} - k_{s_2}\right)} \times \frac{\left((S-1)k_f + k_{s_1}\right) - (S-1)\Phi_1\left(k_f - k_{s_1}\right)}{\left((S-1)k_f + k_{s_1}\right) + \Phi_1\left(k_f - k_{s_1}\right)}$
Heat capacitance $\left(\rho c_p\right)_{hnf}$	$A_6 = \frac{(\rho c_p)_{hnf}}{(\rho c_p)_f} = \left[\left(1 - \Phi_2\right)\left\{\Phi_1 \frac{(\rho c_p)_{s_1}}{(\rho c_p)_f} + \left(1 - \Phi_1\right)\right\} + \Phi_2 \frac{(\rho c_p)_{s_2}}{(\rho c_p)_f}\right]$

$$u_{10}(0) = 1, \quad u_{10}(0) = n_7, \quad u_{12}(0) = n_8, \tag{64}$$

$$u_{13}(0) = 1, \quad u_{13}(0) = n_9, \quad u_{15}(0) = n_{10}. \tag{65}$$

The shooting method is used to estimate the unknowns n_1 to n_{10}. Figure 7 shows the flow chart of solution.

Graphically results and discussion

The main focus is on evaluating dimensionless quantities, such as concentration, velocity, temperature, microorganism $\left(\phi(\xi), \phi_p(\xi), f'(\xi), g'(\xi), \theta(\xi), \theta_p(\xi), \Theta(\xi)\Theta_p(\xi)\right)$ profiles of both phases (I & II) for numerous values of parameters, e.g., $M, \mathrm{Gr}, \mathrm{Gc}, \mathrm{Gn}, \beta,\ \Phi_1, \Phi_2, A^*, B^*, \varepsilon, \mathrm{Rc}, \mathrm{Sr}, \mathrm{Pe}, \Omega,$ and Ma. The range of values for the effective parameters has been chosen by following Mamatha et al. [43], Jawad et al. [47], Khan et al. [48], i.e.,

$$\begin{aligned} &0.1 \le \mathrm{Pe} \le 1.0,\ 0.1 \le \Omega \le 1.0,\ 0.1 \le \beta_\mathrm{m} \le 0.5,\ 1 \le \mathrm{Du} \le 1.8, \\ &\quad 0.1 \le \beta_\mathrm{c} \le 0.5,\ 2 \le \mathrm{Pr} \le 6.9,\ 0.1 \le M \le 4,\ 0.1 \le \mathrm{Gr},\ \mathrm{Gc}, \\ &\quad \mathrm{Gn} \le 1.2,\ 0.1 \le \beta_\mathrm{t} \le 0.5,\ 0.1 \le \beta_\mathrm{v} \le 0.5,\ 0.5 \le \mathrm{Ma} \le 1.2,\ 0.1 \\ &\quad \le \mathrm{Sr} \le 1.6,\ 0.1 \le \mathrm{Rc} \le 1.0,\ 0.1 \le E \le 5,\ 0.1 \\ &\quad \le \mathrm{Le} \le 0.5,\ 0.1 \le \mathrm{Lb} \le 0.5.,\ 0.1 \le A^* \le 1.0. \end{aligned}$$

Figure 8a and b shows variation in flow and thermal profiles of phases (I & II) due to Deborah parameter β. It should be noticed that velocity profiles show a reduction with rising values of β. When β increases cause a reduction in velocity but a rise in $\theta(\xi), \theta_p(\xi)$ for both phases (I & II) because Deborah number is proportional to λ_2(relaxation time). Impact of M on $f'(\xi)$ and $g'(\xi)$ profiles of both phases (I & II) is demonstrated in Fig. 9a. It is noted that as M is increases, the velocity $\left(f'(\xi), g'(\xi)\right)$ profiles of the Jeffry hybrid nanofluid and particle phase decreases. The application of the transverse magnetic field will result in a drag-like resistive force that tends to slow down the velocity of the fluid flow in both phases. In fact, the increase in magnetic parameter results in the decrease of momentum boundary layer thickness. Figures 9b and 10a and b show the influence of Gr, Gc and Gn on velocity profiles of both phases (I & II). For phase-I and phase-II, velocity profiles are improved by increasing the mixed convection parameters. Fe_3O_4 and Cu nanoparticle volume fractions (Φ_1, Φ_2) to have an impact on both $f'(\eta), g'(\eta)$ as shown in Fig. 11a and b. A decreasing effect is shown by increased Φ_1 and Φ_2. Physically, fluid motion slows down as the concentration of nanoparticles in the fluid exceeds the density of the nanofluid, leading to a decrease in velocity profile. The effects of A^* and B^* on $\theta(\xi)$ and $\theta_p(\xi)$ distributions of the hybrid nanofluid phase and the dust phase are portrayed in Figs. 12a and b and 13a and b, respectively. It is found that improving the A^* and B^* values leads to improved thermal distributions for both phases (I & II). When the non-uniform heat sources A^* and B^* are considered to have positive values then it indicates that they transfer heat energy into the fluid flow and cause the temperature distribution to become more uniform. While, non-uniform heat sink A^* and B^* are known as heat sinks when they attain negative values. A certain boundary layer's capacity to absorb heat lowers the temperature in both phases. Variation of temperature profile of phases (I & II) against Φ_1, Φ_2 is shown in Fig. 14a and b. It has been demonstrated that for hybrid nanofluid and nanofluid, the temperatures profiles of both phases (I & II) increase. Physically, more resistance is generated and temperature profiles grow as a result of increasing the values of Φ_1 and Φ_2. The impacts of Du and ε on $\theta(\xi)$ and $\theta_p(\xi)$ for the dust and fluid phases, respectively, are shown in Fig. 15a and b. The impact of Du on $\theta(\xi)$ and $\theta_p(\xi)$ is shown in Fig. 15a. The Dufour effect is used to describe the heat flux caused by a concentration profile. When the Dufour effect is present, the temperature profiles are stronger; while it is absent, it behaves negatively. As the Dufour number rises, the heat boundary layer thickness also dramatically rises, and the boundary layer flow appears to be moreactive. The impact of ε on the thermal profiles is shown in Fig. 15b. Jeffrey hybrid nanofluid and dust phase temperature profiles rise as we raise the value of ε. By raising the values of the variable thermal conductivity parameter, the heating phenomenon is successfully maintained. It has been discovered that using materials with varied thermal properties may accelerate up heat transfer. The effects of Sr and Rc on $\phi(\xi)$ and $\phi_p(\xi)$ for both dust and fluid phases, respectively, are shown in Fig. 16a and b. The graph clearly shows that in Fig. 16a, $\phi(\xi)$ and $\phi_p(\xi)$ drop as Rc increased. The concentration profiles improve when the values of Sr raise. A growth in $\phi(\xi)$ is caused by the increasing Sr, which exhibits increased molar mass diffusivity. The impacts of Ω and Pe on $\Theta(\xi)$ and $\Theta_p(\xi)$ profile of both phases are revealed in Fig. 17a and b. Both the Jeffrey hybrid nanofluid and dust phase microorganism profiles reduced as we raised the Pe and Ω values. The Peclet number (Pe) and cell swimming speed (W_c) are directly related to one another and inversely proportional to D_n (microorganisms diffusivity). The Peclet number affects how quickly advection and diffusion occur. Therefore, a faster rate of advective movement results in a higher Pe, which quickly increases the flux of microorganisms. The effects of Pe increases the swimming rate of motile microorganisms, and this property decreases the thickness of the microorganisms close to the surface of Riga. The impacts of Ma on $\phi(\xi)$, $\phi_p(\xi)$, $f'(\xi)$, $g'(\xi)$, $\theta(\xi)$, $\theta_p(\xi)$, $\Theta(\xi)$ and $\Theta_p(\xi)$ profiles of both the phases (I & II) are illustrated in Figs. 18a and b and 19a and b, respectively. The graph illustrates how raising Ma improves the velocity profiles of

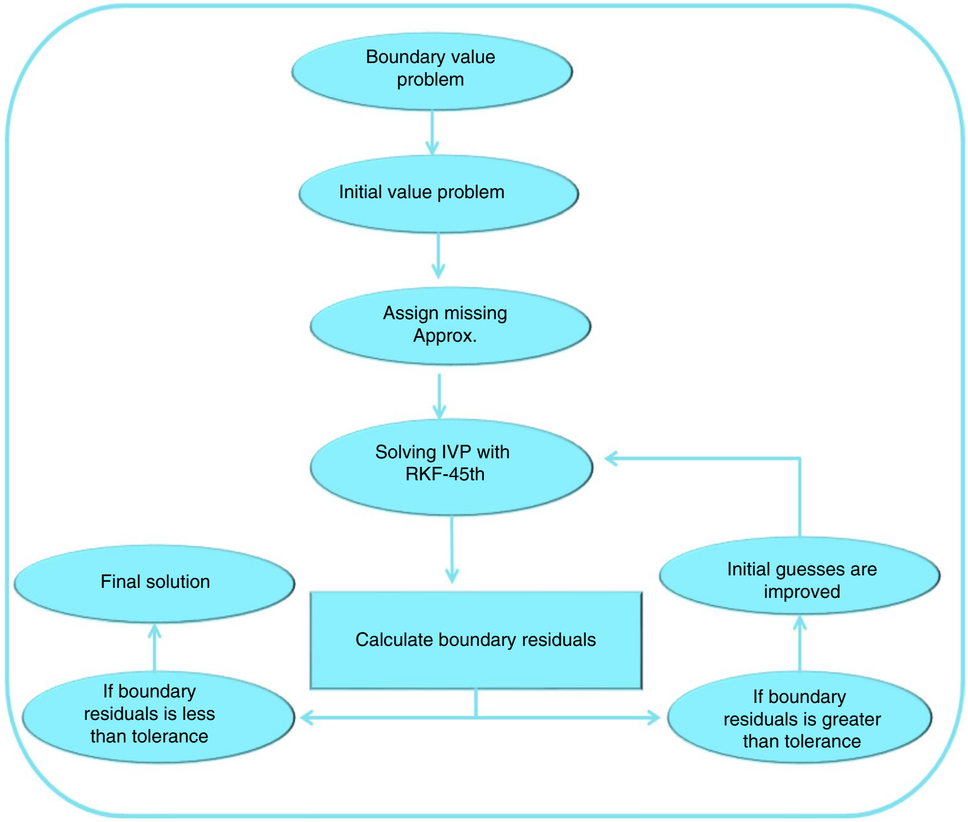

Fig. 7 Flow chart

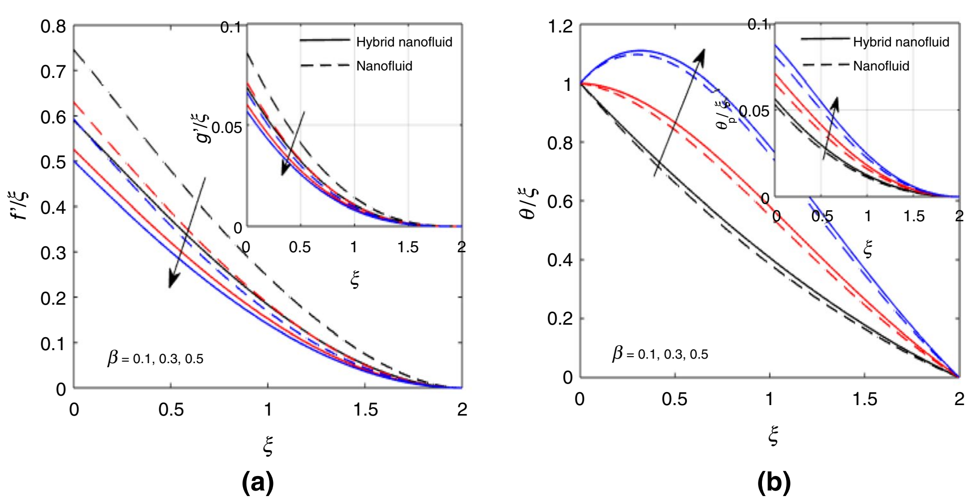

Fig. 8 **a** and **b** Pictogram of $f'(\xi)$, $g'(\xi)$, $\theta(\xi)$, $\theta_p(\xi)$ against β

both the particles and Jeffrey hybrid nanofluid phase. This portent is based on surface variation. A stronger Marangoni influence will almost always lead to a rise in flow profiles for both the phases (I & II). According to these graphs, the thermal, concentration and microorganism profiles significantly decrease as Ma values rise. Surface tension over the surface is induced by the stronger attraction of the liquid to the particles in the geometry. As a result, as surface tension rises, temperature drops. Thermal gradient declines due to the emergence of the surface molecules. As a result, the thermal gradient decreases. The Sherwood and Nusselt numbers are discussed in Tables 3 and 4 in relation to various emergent constraint values. Table 5 uses the integer case and only common factors to compare the mass and microorganism transfer rates between the current study (RKF-45th and BVP4C) and published research (RKF-45th). The current results and earlier results show great agreement.

Fig. 9 **a** and **b** Pictogram of $f'(\xi)$ and $g'(\xi)$ against M and Gr

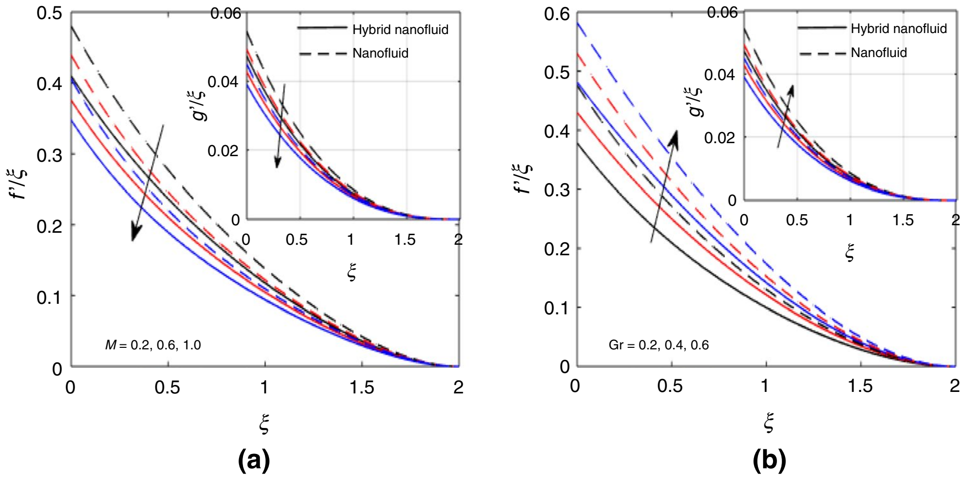

Fig. 10 **a** and **b** Pictogram of $f'(\xi)$ and $g'(\xi)$ against Gc and Gn

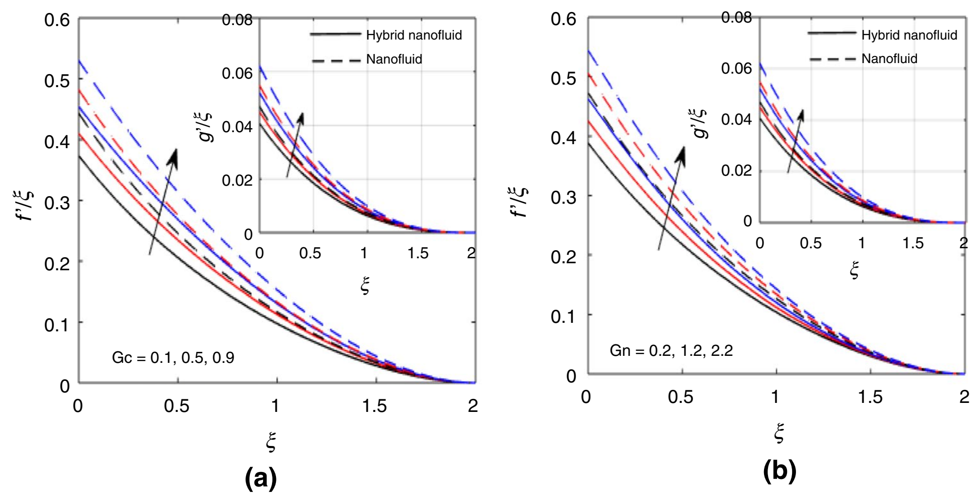

Fig. 11 **a** and **b** Pictogram of $f'(\xi)$ and $g'(\xi)$ against Φ_1 and Φ_2

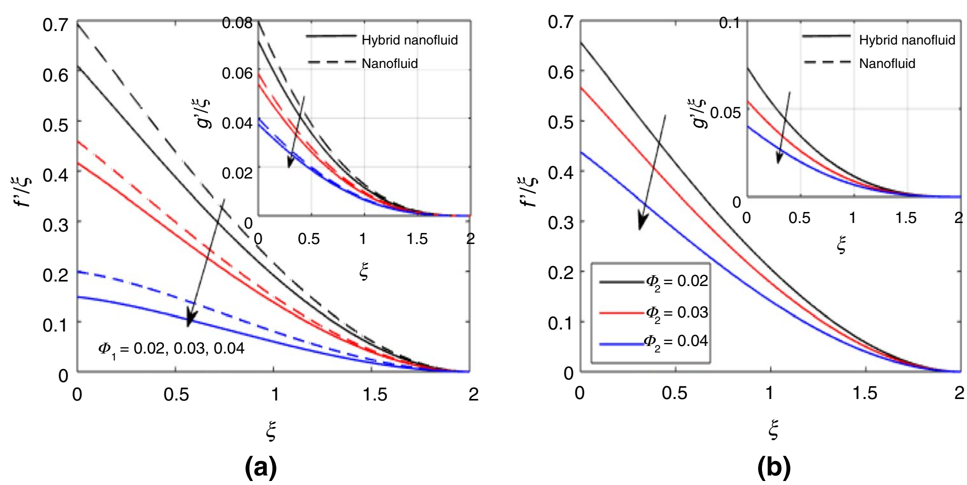

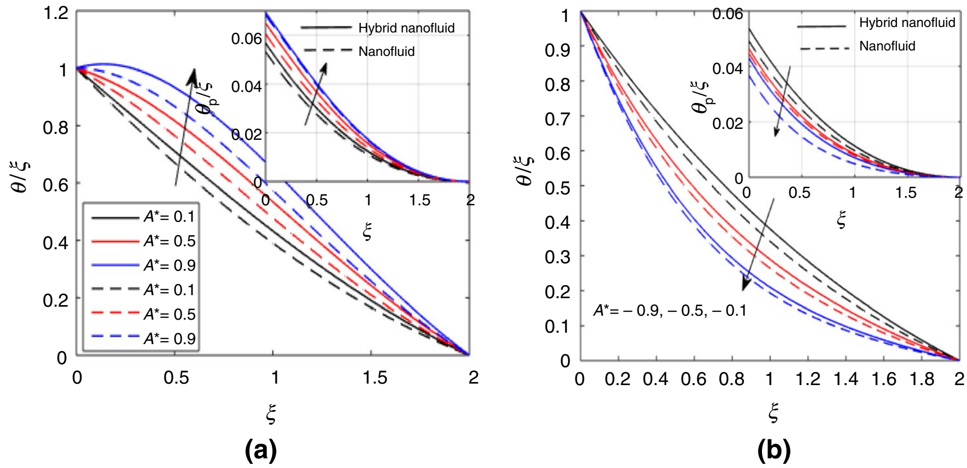

Fig. 12 **a** and **b** Pictogram of $\theta(\xi)$ and $\theta_p(\xi)$ against A^*

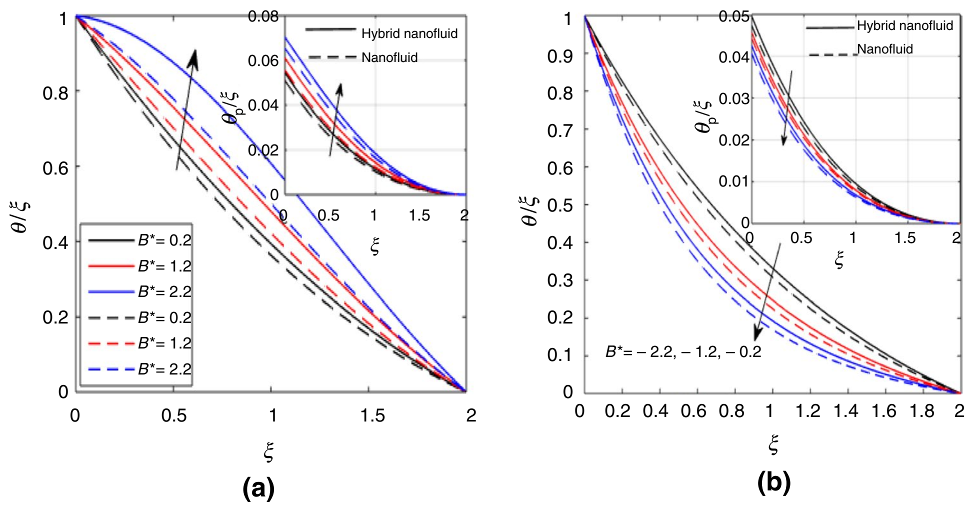

Fig. 13 **a** and **b** Pictogram of $\theta(\xi)$ and $\theta_p(\xi)$ against B^*

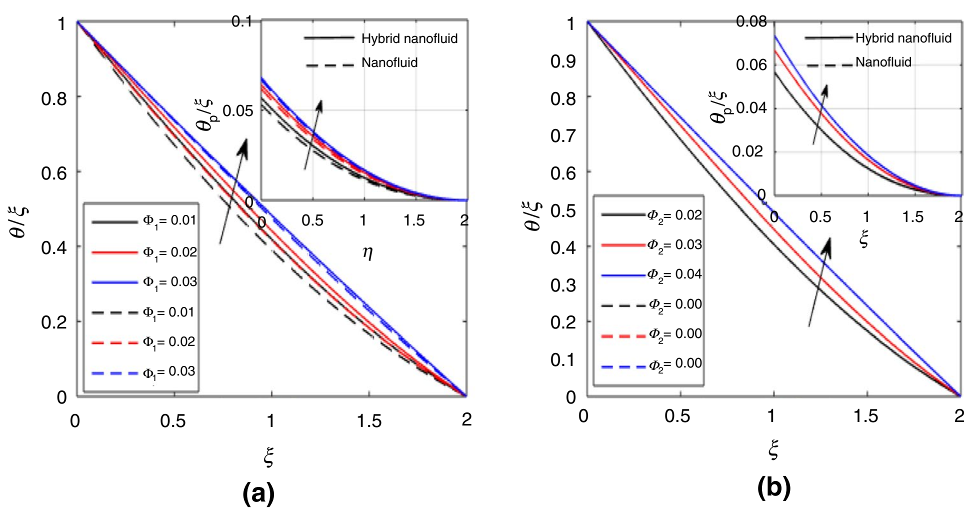

Fig. 14 **a** and **b** Pictogram of $\theta(\xi)$ and $\theta_p(\xi)$ against Φ_1 and Φ_2

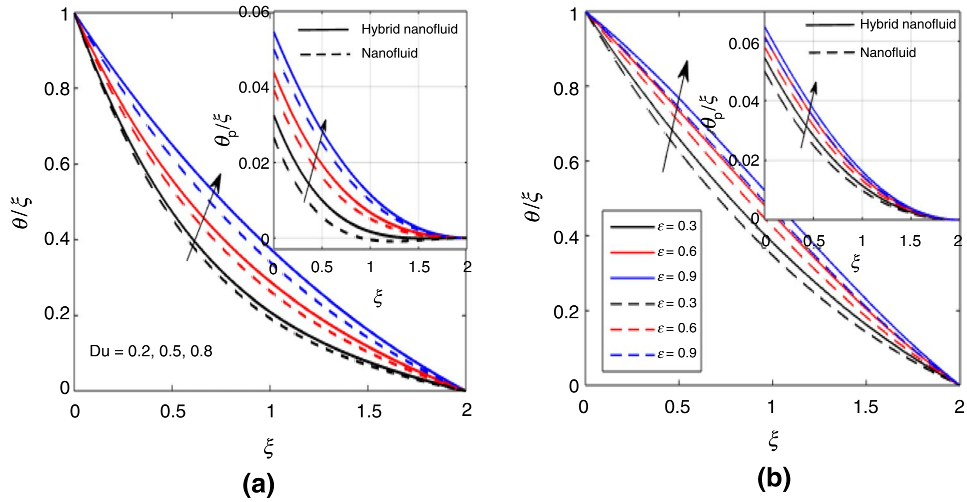

Fig. 15 **a** and **b** Pictogram of $\theta(\xi)$ and $\theta_p(\xi)$ against Du and ε

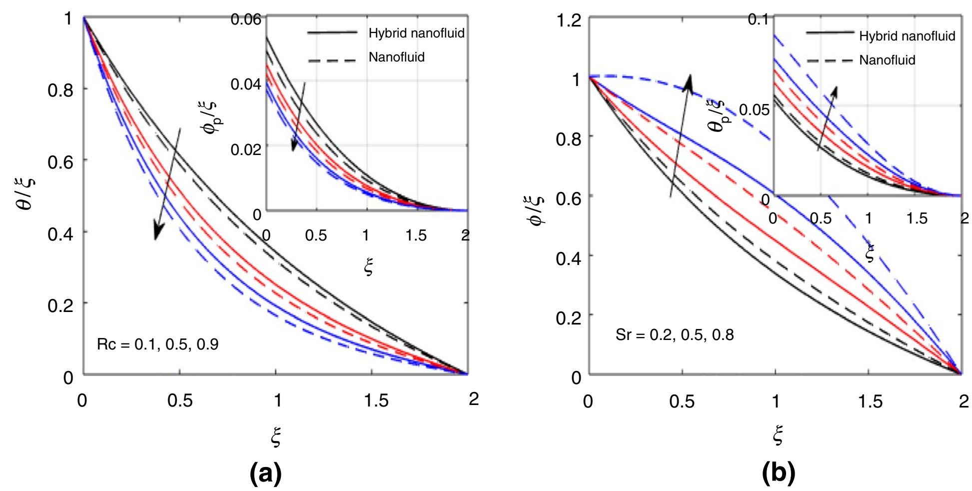

Fig. 16 **a** and **b** Pictogram of $\phi(\xi)$ and $\phi_p(\xi)$ against Rc and Sr

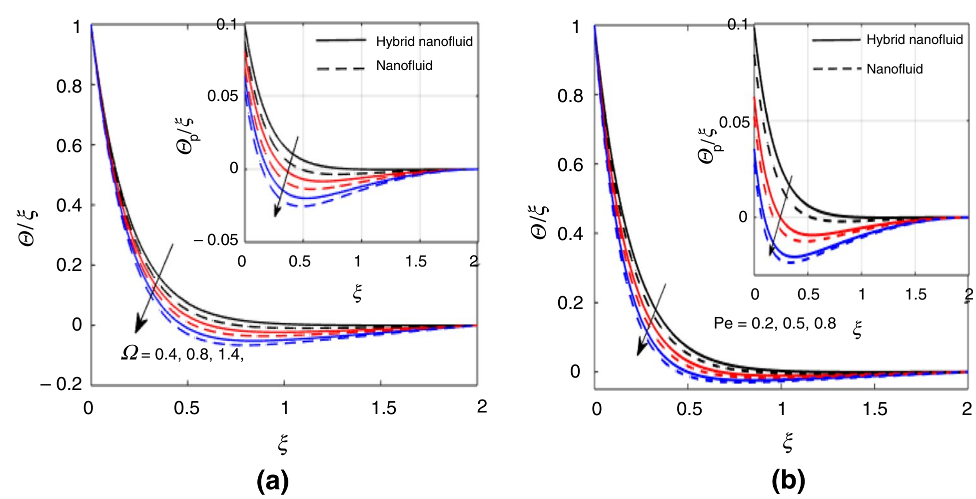

Fig. 17 **a** and **b** Pictogram of $\Theta(\xi)$ and $\Theta_p(\xi)$ against Ω and Pe

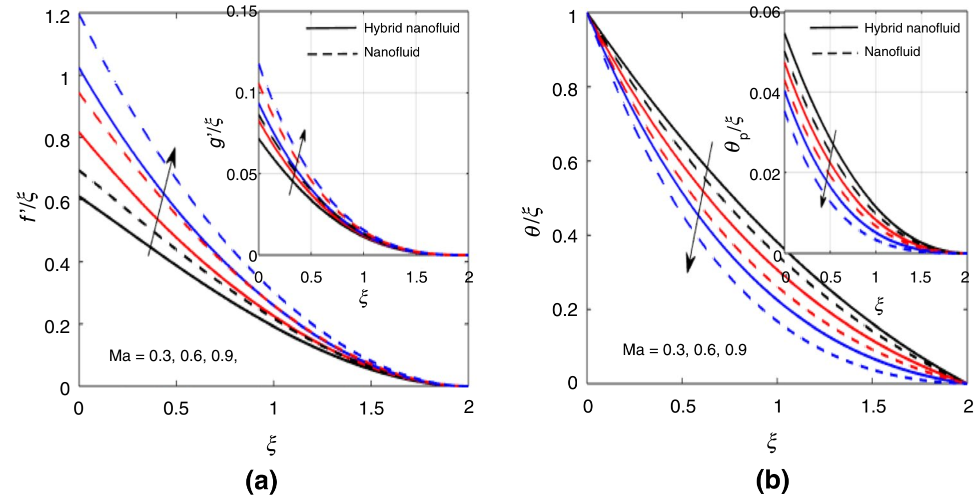

Fig. 18 **a** and **b** Pictogram of $f'(\xi)$, $g'(\xi)$, $\theta(\xi)$ and $\theta_p(\xi)$ against Ma

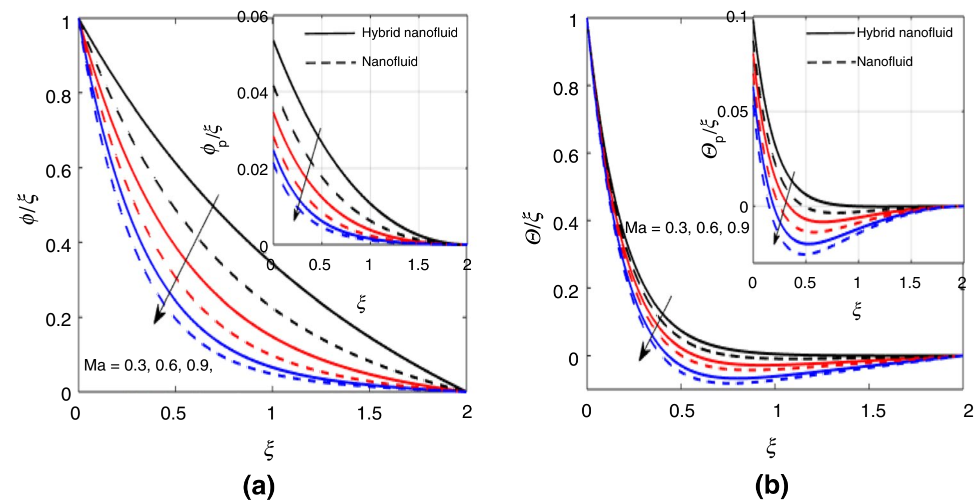

Fig. 19 **a** and **b** Pictogram of $\phi(\xi)$, $\phi_p(\xi)$, $\Theta(\xi)$ and $\Theta_p(\xi)$ against Ma

Table 3 Outcome of various parameters on Nusselt number

Ma	Rd	A^*	B^*	Du	Φ_1	Φ_2	ε	β	Hybrid Nanofluid $Fe_3O_4 + Cu - C_2H_6O_2$ $Nu_x(Re_x)^{-0.5} = -(A_5(1+\varepsilon\theta) + Rd)\theta'(0)$	Nanofluid $Fe_3O_4 - C_2H_6O_2$
1.20	0.3	0.4	0.1	0.6	0.03	0.04	0.4	0.5	7.334001	6.807067
1.26									7.625977	6.819267
1.32									7.994194	6.831029
	0.3								7.814246	6.807136
0.4	**0.4**	0.3	0.1	0.6	0.03	0.04	0.4	0.5	10.323843	9.318319
	0.5								12.833355	11.829398
		0.2							7.814246	6.807136
0.1	2.0	**0.3**	0.1	0.6	0.03	0.04	0.4	0.5	7.814476	6.807331
		0.4							7.814712	6.807530
			0.2						7.814246	6.807136
0.2	2.0	0.3	**0.3**	0.6	0.03	0.04	0.4	0.5	7.816666	6.808569
			0.4						7.829186	6.811991
				0.2					6.235025	5.480029
0.2	2.0	0.3	0.1	**0.3**	0.03	0.04	0.4	0.5	6.234790	5.479776
				0.4					6.234546	5.479512
					0.02				6.235025	5.480029
0.2	2.0	0.3	0.1	0.6	**0.04**	0.04	0.4	0.5	8.871231	7.692014
					0.06				13.319607	11.425857
						0.01			6.235025	…
0.2	2.0	0.3	0.1	0.6	**0.06**	**0.02**	0.4	0.5	10.549007	…
						0.03			17.294222	…
							0.2		5.445301	4.816325
0.2	2.0	0.3	0.1	0.6	0.03	0.04	**0.4**	0.5	6.235025	5.480029
							0.6		7.024761	6.143743
								0.1	7.814507	6.807466
0.2	2.0	0.3	0.1	0.6	0.03	0.04	0.4	**0.2**	7.810594	6.803553
								0.3	7.809028	6.802007

Table 4 Effect of many parameters on Sherwood number

Ma	Sr	Rc	Le	E	Φ_1	Φ_2	Hybrid Nanofluid $Fe_3O_4 + Cu - C_2H_6O_2$ $Sh_x = -(Re)^{1/2}\phi'(0)$	Nanofluid $Fe_3O_4 + Cu - C_2H_6O_2$
1.20	0.3	0.4	0.1	0.6	0.05	0.04	2.516062	2.518598
1.26							2.587621	2.524670
1.32							2.696021	2.530528
	0.3						2.516160	2.518760
0.2	**0.6**	0.3	0.1	0.6	0.05	0.04	2.516577	2.519341
	0.9						2.517030	2.519986
		0.2					2.516160	2.518760
0.2	2.0	**0.3**	0.1	0.6	0.05	0.04	2.515970	2.518551
		0.4					2.515792	2.518356
			0.1				2.516160	2.518760
0.2	2.0	0.3	**0.3**	0.6	0.05	0.04	2.511423	2.513407
			0.4				2.508796	2.510403
				0.02			2.516160	2.518760
0.2	2.0	0.3	0.1	**0.4**	0.05	0.04	2.516184	2.518785
				0.6			2.516193	2.518796
					0.02		2.536360	1.519413
0.2	2.0	0.3	0.1	0.6	**0.04**	0.04	2.526160	1.505533
					0.06		2.516260	1.496203
						0.01	2.516160	…
						0.03	2.509787	…
0.2	2.0	0.3	0.1	0.6	0.05	**0.05**	2.506013	…

Table 5 The comparison results of the present study to earlier published research, with the additional parameters set to zero

				Nn_x(local density of motile microorganisms)			Sh_x(Sherwood number)		
L	Pe	β_c	β_m	Present results		Mamatha et al. [43]	Present results		Mamatha et al. [43]
				RKF-45th	BVP4C	RK	RKF-45th	BVP4C	RK
0.01				0.042428	0.042420	0.042425	0.035712	0.035706	0.035707
0.05				0.042930	0.042924	0.042925	0.045354	0.045340	0.045347
0.1				0.044026	0.044016	0.044018	0.057547	0.057540	0.057542
	0.3			0.026350	0.026340	0.026348	0.084820	0.084810	0.084815
	0.5			0.035536	0.035530	0.035530	0.084822	0.084812	0.084815
	0.7			0.045556	0.045550	0.045550	0.084823	0.084812	0.084815
		0.1		0.044252	0.044245	0.044245	0.103894	0.103890	0.103889
		0.2		0.060508	0.060500	0.060505	0.126256	0.126250	0.126251
		0.3		0.070240	0.070236	0.070232	0.139279	0.139274	0.139274
			0.1	0.108978	0.108970	0.108973	0.183969	0.183964	0.183965
			0.2	0.105906	0.105900	0.105902	0.183969	0.183964	0.183965
			0.3	0.104440	0.104430	0.104438	0.183969	0.183964	0.183965

Conclusions

The thermo-solutal Marangoni convective flow of a dusty MHD Jeffrey hybrid nanofluid including microorganisms with heat source and activation energy over a Riga plate has been examined numerically in the present investigation. The following are the main outcomes of the investigation:

- The velocity profiles, Nusselt number and Sherwood number enhance due to an increase in Marangoni convection parameter, while converse behavior is found for, thermal, microorganisms and concentration profiles for both phases. The Marangoni number surface tension has a significant impact. Surface tension is a result of a liquid's bulk attraction to the particles in the surface layer on its surface. As a result, the temperature decreases as the surface tension increases, and the bulk magnetism between the surface molecules rises or intensifies.

- The phases (I&II) of velocity profiles get declined and thermal profiles enhance for higher values of volume friction of nanoparticles. Physically, fluid motion slows down as the concentration of nanoparticles in the fluid exceeds the density of the nanofluid, leading to a decrease in velocity profiles.
- The concentration profiles decrease as chemical reaction parameter levels rise, while Soret number exhibits the opposite behavior.
- For larger values of Peclet number, the density of hybrid nanofluid and nanofluid motile microorganisms profiles decreases. The effects of Peclet number increases the swimming rate of motile microorganisms, and this property decreases the thickness of the microorganisms close to the surface of Riga.
- By increasing the value of Marangoni convection parameter up to 10% the values of heat transfer and mass transfer enhance up to 9% and 7.15%, respectively.

Future work

Future research should expand on this work by taking into account thermophoresis particle deposition, convective conditions, variable conditions and trihybrid nanoparticles. These models will be highly helpful in the construction of furnaces, atomic power plants, gas-cooled nuclear reactors, SAS turbines, and unique driving mechanisms for aircraft, rockets, satellites, and spacecraft.

References

1. Pearson JR. On convection cells induced by surface tension. J Fluid Mech. 1958;4(5):489–500.
2. Abbas M, Khan N, Shehzad SA. Thermophoretic particle deposition in Carreau-Yasuda fluid over chemical reactive Riga plate. Adv Mech Eng. 2023;15(1):16878132221135096.
3. Mat NA, Arifin NM, Nazar R, Ismail F. Radiation effect on Marangoni convection boundary layer flow of a nanofluid. Math Sci. 2012;6:1–6.
4. Al-Sharafi A, Sahin AZ, Yilbas BS, Shuja SZ. Marangoni convection flow and heat transfer characteristics of water–CNT nanofluid droplets. Numer Heat Trans Part A Appl. 2016;69(7):763–80.
5. Khan M, Salahuddin T, Malik MY, Alqarni MS, Alqahtani AM. Numerical modeling and analysis of bioconvection on MHD flow due to an upper paraboloid surface of revolution. Phys A. 2020;553:124231.
6. Chu YM, Al-Khaled K, Khan N, Khan MI, Khan SU, Hashmi MS, Iqbal MA, Tlili I. Study of Buongiorno's nanofluid model for flow due to stretching disks in presence of gyrotactic microorganisms. Ain Shams Eng J. 2021;12(4):3975–85.
7. Hill NA, Bees MA. Taylor dispersion of gyrotactic swimming micro-organisms in a linear flow. Phys Fluids. 2002;14(8):2598–605.
8. Khan N, Riaz I, Hashmi MS, Musmar SA, Khan SU, Abdelmalek Z, Tlili I. Aspects of chemical entropy generation in flow of Casson nanofluid between radiative stretching disks. Entropy. 2020;22(5):495.
9. Khan N, Nabwey HA, Hashmi MS, Khan SU, Tlili I. A theoretical analysis for mixed convection flow of Maxwell fluid between two infinite isothermal stretching disks with heat source/sink. Symmetry. 2019;12(1):62.
10. Raju CS, Hoque MM, Sivasankar T. Radiative flow of Casson fluid over a moving wedge filled with gyrotactic microorganisms. Adv Powder Technol. 2017;28(2):575–83.
11. Reddy MG, Kumar N, Prasannakumara BC, Rudraswamy NG, Kumar KG. Magnetohydrodynamic flow and heat transfer of a hybrid nanofluid over a rotating disk by considering Arrhenius energy. Commun Theor Phys. 2021;73(4):045002.
12. Khan NS, Kumam P, Thounthong P. Second law analysis with effects of Arrhenius activation energy and binary chemical reaction on nanofluid flow. Sci Rep. 2020;10(1):1226.
13. Hussain Z, Hussain A, Anwar MS, Farooq M. Analysis of Cattaneo–Christov heat flux in Jeffery fluid flow with heat source over a stretching cylinder. J Therm Anal Calorim. 2022;1–12.
14. Khan MI, Alzahrani F. Nonlinear dissipative slip flow of Jeffrey nanomaterial towards a curved surface with entropy generation and activation energy. Math Comput Simul. 2021;185:47–61.
15. Hakeem AK, Nayak MK, Makinde OD. Effect of exponentially variable viscosity and permeability on Blasius flow of Carreau nano fluid over an electromagnetic plate through a porous medium. J Appl Comput Mech. 2019;5(2):390–401.
16. Saranya S, Ragupathi P, Ganga B, Sharma RP, Hakeem AA. Nonlinear radiation effects on magnetic/non-magnetic nanoparticles with different base fluids over a flat plate. Adv Powder Technol. 2018;29(9):1977–90.
17. Hakeem AA, Saranya S, Ganga B. Comparative study on Newtonian/non-Newtonian base fluids with magnetic/non-magnetic nanoparticles over a flat plate with uniform heat flux. J Mol Liq. 2017;230:445–52.
18. Ganesh NV, Hakeem AA, Ganga B. A comparative theoretical study on Al_2O_3 and γ-Al_2O_3 nanoparticles with different base fluids over a stretching sheet. Adv Powder Technol. 2016;27(2):436–41.
19. Rashidi MM, Ganesh NV, Hakeem AA, Ganga B. Buoyancy effect on MHD flow of nanofluid over a stretching sheet in the presence of thermal radiation. J Mol Liq. 2014;198:234–8.
20. Hashmi MS, Al-Khaled K, Khan N, Khan SU, Tlili I. Buoyancy driven mixed convection flow of magnetized Maxell fluid with homogeneous-heterogeneous reactions with convective boundary conditions. Res Phys. 2020;19:103379.
21. Aldabesh A, Hussain M, Khan N, Riahi A, Khan SU, Tlili I. Thermal variable conductivity features in Buongiorno nanofluid model between parallel stretching disks: improving energy system efficiency. Case Stud Therm Eng. 2021;23:100820.
22. Abdelsalam SI, Alsharif AM, Abd EY, Abdellateef AI. Assorted kerosene-based nanofluid across a dual-zone vertical annulus with electroosmosis. Heliyon. 2023;9(5).
23. Abd EY. Two-layered electroosmotic flow through a vertical microchannel with fractional Cattaneo heat flux. J Taibah Univ Sci. 2021;15(1):1038–53.
24. Abbas M, Khan N, Hashmi MS, Younis J. Numerically analysis of Marangoni convective flow of hybrid nanofluid over an infinite disk with thermophoresis particle deposition. Sci Rep. 2023;13(1):5036.

25. Acharya N. Magnetized hybrid nanofluid flow within a cube fitted with circular cylinder and its different thermal boundary conditions. J Magn Magn Mater. 2022;564:170167.
26. Acharya N. On the hydrothermal behavior and entropy analysis of buoyancy driven magnetohydrodynamic hybrid nanofluid flow within an octagonal enclosure fitted with fins: application to thermal energy storage. J Energy Storage. 2022;53:105198.
27. Acharya N, Mabood F, Badruddin IA. Thermal performance of unsteady mixed convective Ag/MgO nanohybrid flow near the stagnation point domain of a spinning sphere. Int Commun Heat Mass Transf. 2022;134:106019.
28. Hopkinson N, Dicknes P. Analysis of rapid manufacturing—using layer manufacturing processes for production. Proc Inst Mech Eng C J Mech Eng Sci. 2003;217(1):31–9.
29. Acharya N. On the flow patterns and thermal control of radiative natural convective hybrid nanofluid flow inside a square enclosure having various shaped multiple heated obstacles. Eur Phys J Plus. 2021;136(8):889.
30. Postelnicu A. Heat and mass transfer by natural convection at a stagnation point in a porous medium considering Soret and Dufour effects. Heat Mass Transf. 2010;8(46):831–40.
31. Srinivasacharya D, RamReddy C. Soret and Dufour effects on mixed convection in a non-Darcy porous medium saturated with micropolar fluid. Nonlinear Anal Model Control. 2011;16(1):100–15.
32. Ramzan M, Bilal M, Chung JD. Soret and Dufour effects on three dimensional upper-convected Maxwell fluid with chemical reaction and non-linear radiative heat flux. Int J Chem Reactor Eng. 2017;15(3):20160136.
33. Khan N, Riaz M, Hashmi MS, Khan SU, Tlili I, Khan MI, Nazeer M. Soret and Dufour features in peristaltic motion of chemically reactive fluid in a tapered asymmetric channel in the presence of Hall current. J Phys Commun. 2020;4(9):095009.
34. Sulochana C, Payad SS, Sandeep N. Non-uniform heat source or sink effect on the flow of 3D Casson fluid in the presence of Soret and thermal radiation. Int J Eng Res Afr. 2016;20:112–29.
35. Ramzan M, Yousaf F, Farooq M, Chung JD. Mixed convective viscoelastic nanofluid flow past a porous media with Soret—DuFour effects. Commun Theor Phys. 2016;66(1):133.
36. Ragupathi P, Hakeem AA, Al-Mdallal QM, Ganga B, Saranya S. Non-uniform heat source/sink effects on the three-dimensional flow of Fe3O4/Al2O3 nanoparticles with different base fluids past a Riga plate. Case Stud Therm Eng. 2019;15:100521.
37. Nayak MK, Hakeem AA, Ganga B. Influence of non-uniform heat source/sink and variable viscosity on mixed convection flow of third grade nanofluid over an inclined stretched Riga plate. Int J Thermofluid Sci Technol. 2019;6(4):19060401.
38. Abdul Hakeem AK, Ragupathi P, Saranya S, Ganga B. Three dimensional non-linear radiative nanofluid flow over a Riga plate. J Appl Comput Mech. 2020;6(4):1012–29.
39. Ragupathi P, Saranya S, Hakeem AA, Ganga B. Numerical analysis on the three-dimensional flow and heat transfer of multiple nanofluids past a Riga plate. In: Journal of Physics: Conference Series 2021;012044.
40. Riaz M, Khan N, Shehzad SA. Rheological behavior of magnetized ZnO–SAE 50 nanolubricant over Riga plate: a theoretical study. Adv Mech Eng. 2023;15(3):16878132231162304.
41. Riaz M, Khan N, Hashmi MS, Younis J. Heat and mass transfer analysis for magnetized flow of ZnO-SAE 50 nanolubricant with variable properties: an application of Cattaneo-Christov model. Sci Rep. 2023;13(1):8717.
42. Riaz M, Khan N. A numerical approach to the modeling of Thompson and Troian slip on magnetized flow of Al 2 O3 –PAO nanolubricant over an inclined rotating disk. Adv Mech Eng. 2023;15(6):16878132231183926.
43. Mamatha SU, Ramesh Babu K, Durga Prasad P, Raju CSK, Varma SVK. Mass transfer analysis of two-phase flow in a suspension of microorganisms. Arch Thermodyn. 2020;175–92.
44. Obalalu AM, Ajala OA, Abdulraheem A, Akindele AO. The influence of variable electrical conductivity on non-Darcian Casson nanofluid flow with first and second-order slip conditions. Partial Differ Equ Appl Math. 2021;4:100084.
45. Gorla R. Two-phase boundary layer flow, heat and mass transfer of a dusty liquid past a stretching sheet with thermal radiation. Int J Ind Math. 2016;8(3):279–92.
46. Unyong B, Vadivel R, Govindaraju M, Anbuvithya R, Gunasekaran N. Entropy analysis for ethylene glycol hybrid nanofluid flow with elastic deformation, radiation, non-uniform heat generation/absorption, and inclined Lorentz force effects. Case Stud Therm Eng. 2022;30:101639.
47. Jawad M, Saeed A, Kumam P, Shah Z, Khan A. Analysis of boundary layer MHD Darcy-Forchheimer radiative nanofluid flow with soret and dufour effects by means of marangoni convection. Case Stud Therm Eng. 2021;23:100792.
48. Khan MI, Alzahrani F, Hobiny A. Heat transport and nonlinear mixed convective nanomaterial slip flow of Walter-B fluid containing gyrotactic microorganisms. Alex Eng J. 2020;59(3):1761–9.

Publisher's Note Springer Nature remains neutral with regard to jurisdictional claims in published maps and institutional affiliations.